Metabolism-weighted brain connectome reveals synaptic integration and vulnerability to neurodegeneration

Mahnaz Ashrafi[1], Laura Fraticelli[1,2], Gabriel Castrillón[1,2,3], Valentin Riedl[1,2]

1 Department of Neuroradiology, University Hospital TUM Klinikum, Technical University of Munich, Munich, Germany

2 Department of Neuroradiology, Universitätsklinikum, Friedrich-Alexander-University Erlangen-Nuernberg, Erlangen, Germany

3 Research Group in Medical Imaging, SURA Ayudas Diagnósticas, Medellín, Colombia

ABSTRACT

The remarkable abilities of the human brain arise from its specialized regions, which process and integrate information through complex connectivity patterns. While network science has developed various metrics to assess the degree of connectivity between these regions, it has not yet considered the level of activity within each region. Consequently, a highly connected region might be classified as a hub in the brain's connectome, even if it is weakly active or linked primarily to less active areas. Conversely, a region that is highly active but has only a few connections may be undervalued. To address this issue, we present a fully-weighted brain graph in which both edges (representing connectivity) and nodes (indicating metabolic activity) contribute to the importance, or centrality, of each region. In this model, the metabolism-weighted centrality (MwC) of each brain region integrates both connectivity and metabolic activity, using three datasets from simultaneously acquired functional MRI and metabolic FDG-PET data. We found that our fully-weighted brain graph demonstrates a greater ability to explain quantitative imaging data of signaling metabolism and its association with cognitive domains than a classical, edge-weighted graph. Additionally, regions with relatively high MwC exhibited increased synaptic and metabolic activity, as indicated by transcriptomic data. Furthermore, these regions showed higher susceptibility to neurodegenerative disorders. This framework of a fully-weighted brain graph represents a paradigm shift from connectivity-based metrics to an activity-aware brain graph. It offers a more biologically informed representation of brain network dynamics, connecting metabolic activity levels to higher cognitive functions as well as neurodegeneration.

INTRODUCTION

The human brain consists of anatomically distinct regions, each characterized by unique structural, functional, and biological characteristics. Nevertheless, the extensive range of human cognitive functions arises from the interconnectivity among these specialized regions (Menon, 2011; Park & Friston, 2013; Sporns, 2011). The emphasis on the connectome to understand the unique attributes of the brain or to describe alterations associated with certain disorders represents a significant shift in neuroscience. This progress is largely due to network science, which provides a framework for representing the connectome as a graph, wherein nodes correspond to individual brain regions and edges represent their structural or functional connections (Bressler & Menon, 2010; E. Bullmore & Sporns, 2009; E. T. Bullmore & Bassett, 2011; Craddock et al., 2013; De Vico Fallani et al., 2012; Zalesky et al., 2010).

A notable drawback of conventional graph models, known as edge-weighted graphs, is that the node characteristics and importance within the network architecture are deduced from their edge weights, while treating nodes themselves as homogenous entities (E. Bullmore & Sporns, 2009; Rubinov & Sporns, 2010; Sporns, 2018). Degree centrality (DC), for instance, serves as a widely utilized graph metric that identifies network hubs solely based on the quantity of their edges (Kuhnert et al., 2012; Kwon et al., 2019; J. Zhang et al., 2020). Importantly, these edge-weighted models overlook regional differences in metabolic and signaling activities, which are crucial for understanding signal propagation and integration along the network architecture. This shortcoming is particularly concerning when exploring the connectome in the context of neurological or psychiatric disorders. For instance, in Alzheimer's disease, regional vulnerability is mainly influenced by local metabolic activity, rather than connectivity in isolation (Sanabria-Diaz et al., 2013; Arnemann et al., 2018; Lin et al., 2023). Consequently, an edge-focused perspective on the brain connectome neglects region-specific characteristics of signaling activity or metabolism. A limited number of brain imaging studies have used nodal information to delineate subnetworks based on the similarities of nodal characteristics (Murphy et al., 2016; Bassett & Sporns, 2017; Bazinet et al., 2023; Hansen et al., 2023). Still, the graph metrics in these studies have been computed utilizing edge information alone.

Recent developments in network science effectively address these limitations by proposing a new generation of graph models that incorporate node attributes into conventional network frameworks, thereby facilitating a more exact delineation of a node's topological importance (Kivela et al., 2014; Boccaletti et al., 2014; Heitzig et al., 2012; Wiedermann et al., 2013; Giustolisi et al., 2020; Abbasi & Hossain, 2013; Singh et al., 2020). One prominent approach is node-weighted centrality, which allocates weights to both nodes and edges, thereby redefining traditional centrality assessments (Abbasi & Hossain, 2013). In contrast to techniques that depend solely on edge weights, node-weighted centrality integrates the inherent characteristics or activity levels of the nodes themselves. To exemplify, consider the evaluation of the significance of stations within a subway network. An edge-oriented perspective might suggest that a station with numerous connections is central within the subway graph. However, this view can be misleading if it ignores factors like low passenger numbers or infrequent train service, which indicate low activity at that station. In contrast, a station with fewer connections but a high volume of passengers may actually serve a more central role in the subway system’s overall function. Consequently, including nodal information, such as passenger counts or train frequency, yields a more accurate assessment of each station's true significance within the subway network. When applying this concept to the brain connectome, the level of signal integration at a specific node cannot be fully characterized by just considering the degree of edges; it needs to additionally incorporate the level of activity in connected regions.

In this study, we present the first fully-weighted brain graph that integrates edge weights with the level of nodal activity. This offers an activity-driven representation of the brain connectome rather than solely relying on the topological degree of edges. Approximately 80% of neuronal energy metabolism is associated with signaling activity and, specifically, synaptic signal integration (Attwell & Laughlin, 2001; Harris et al., 2012; Karbowski, 2012; Hyder et al., 2013). Thus, regional energy metabolism serves as a biologically reliable metric of a region's signaling

activities throughout its connections. We utilized simultaneously acquired data on cortical energy metabolism, obtained through [^{18}F]FDG-PET, in conjunction with brain connectivity data from BOLD fMRI, to compute a biologically informed metric of nodal signaling dominance, which we designated as Metabolism-weighted Centrality (MwC). The MwC metric effectively summarizes the cumulative information processing of a specific region, deduced by the signaling activities of all connected regions. A high MwC value signifies regions that are influenced by metabolically active neighbors, indicating enhanced integration capacity within the network. Conversely, low MwC values denote regions connected to metabolically less active neighbors, suggesting diminished signal integration or reduced functional impact.

RESULTS

Metabolism-weighted centrality (MwC) indicates regions with high signaling dominance in a fully-weighted brain graph

We analyzed three independent datasets, each acquired on an integrated PET/MRI scanner at two different sites (TUM University Hospital Munich, Medical University of Vienna). The main dataset included 20 healthy subjects (10 females, age: 34.5 ± 5 years, TUM), and the two replication datasets comprised 10 subjects each (5 females, age: 27 ± 5 years, TUM.rep; 5 females, age: 27 ± 7 years, Vienna). All datasets provide simultaneously acquired measures of metabolic activity (cerebral metabolic rate of glucose, CMRglc) from FDG-PET and of functional connectivity (FC) from fMRI data. We performed all analyses in subject space and modeled the brain graph on regions as defined by the Human Connectome Project Multimodal Parcellation (HCP MMP) atlas (Fig. 1a) (Glasser et al., 2016).

The fully-weighted brain graph is defined as a two-layer network, including the energy metabolism in each region (Fig. 1b) and the FC matrix of correlated BOLD signal time-series for each pair of regions (Fig. 1c). We then calculated MwC for each node *t* as:

$$MwC(t) = \sum_{i=1}^{N} nFC(t,i) \times E(i)$$

where *t* is the target region, *N* is the total number of regions connected to node *t*, *nFC(t,i)* is the normalized FC between nodes *t* and *i*, and *E(i)* is the energy metabolism of any connected region *i*. *nFC* is calculated by dividing the FC value between nodes *t* and *i* by the total sum of connections linked to node *t*. This normalization reflects the relative influence of each connected region *i* on the activity of region *t* (see Methods).

The region-wise calculation of MwC results from a fully-weighted brain graph that incorporates both the connectivity profile and the metabolic activity of connected regions (Fig. 1d). In contrast, the classical model of DC is calculated solely as the sum of weighted edges for a given region *t*, without considering varying levels of activity in connected nodes (Fig. 1e). The toy example in Fig. 1f illustrates the critical difference between the two centrality measures for two arbitrary nodes, t_1 and t_2. Using an edge-weighted model only, the two nodes have the same DC and are thus

ranked with equal centrality (lower panel). MwC, on the other hand, additionally considers the level of activity in connected regions 1 to 3, which results in a biologically more realistic model of information processing along the network. In our example, t_1 has a higher centrality within the brain connectome as it connects to nodes with higher activity than t_2 (upper panel).

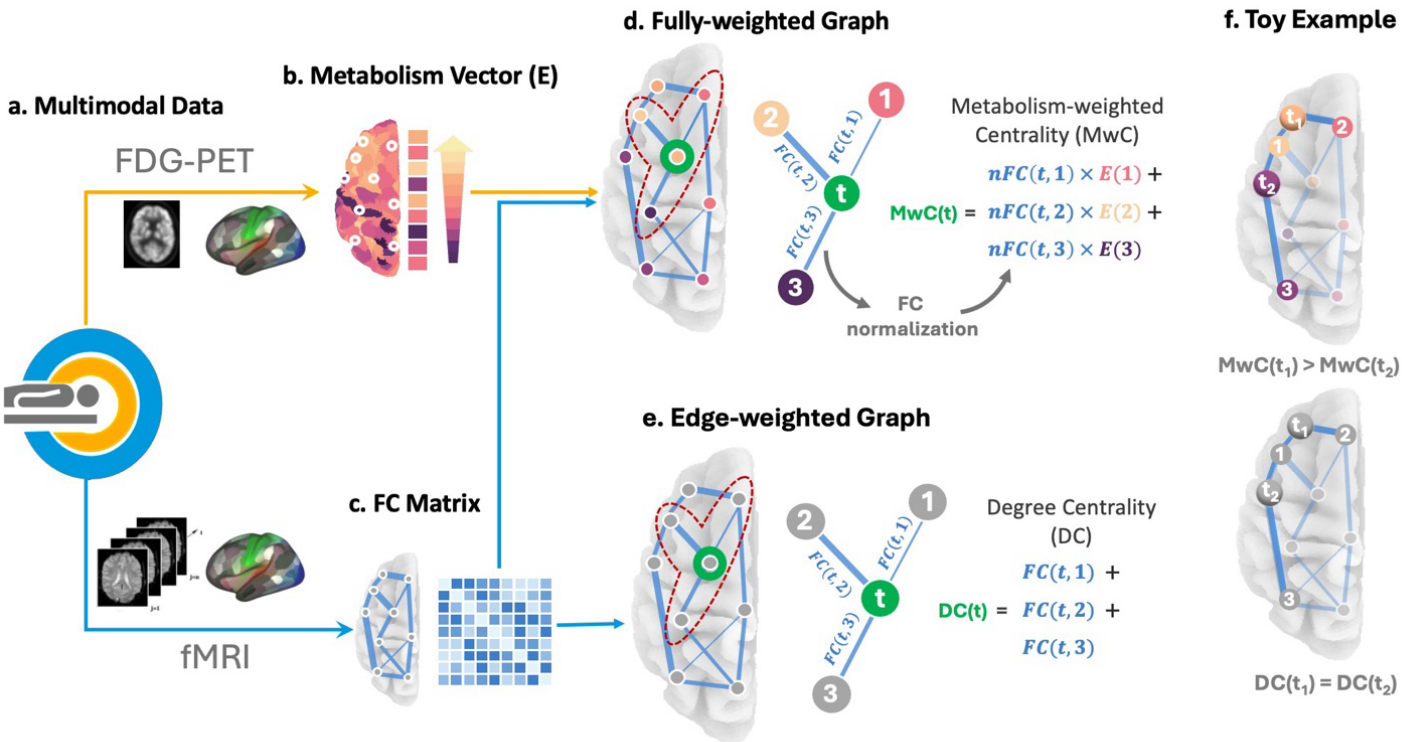

Fig1: Calculation of MwC and DC. (a) FDG-PET (orange) and fMRI (blue) data were acquired simultaneously on an integrated PET/MRI scanner and parcellated according to 360 ROIs from the Human Connectome Project Multi-Modal Parcellation (HCP MMP) atlas. **(b)** Brain surface representation of energy metabolism (CMRglc) across the cortex. Each white circle represents a region where the median CMRglc value is extracted and stored in a vector of energy metabolism *E*, color-coding the metabolic activity. **(c)** A network graph overlaid on the brain illustrates the brain FC profile. Nodes represent brain regions, with edge thickness indicating the weighted FC strength, calculated as the statistical dependencies between pairwise nodal fMRI time series and plotted as an FC matrix. The connectivity matrix is used to calculate both the MwC and DC. **d)** Fully-weighted graph where the color-coded node values correspond to the values of vector *E* in b) and its edges, the FC matrix in c). The inset illustrates the MwC of a target region t in green, connected to three regions (1-3) highlighted by the dashed red contour, as the sum of the product between *E(i)* and *nFC(t,i)* across its connected nodes. **(e)** Using an edge-weighted graph, the DC is calculated as the sum of the FC of all connected nodes from fMRI data only. **(f)** Case scenario of two regions, t_1 and t_2, with identical DC values (lower panel) but different metabolic profiles. Both nodes are connected to region 1, but region t_1 is additionally connected to 2, and region t_2 to region 3, which have different metabolism profiles (*E(2) > E(3)*), shown in the upper panel. Integrating nodal metabolism into the model yields different MwC ($MwC(t_1) > MwC(t_2)$) while they have identical DC ($DC(t_1) = DC(t_2)$).

MwC describes the cortical energy distribution better than DC

After calculating both graph metrics, we examined how well each centrality measure matches the signaling-related energy metabolism across the cortex. We calculated the correlations of MwC and DC with CMRglc across brain regions and compared their performance. It is important to note that the calculation of MwC for node *t* is independent of *E(t)*, as it only uses the CMRglc from connected regions *i*.

On the group level, the subject average CMRglc shows a significant positive correlation with MwC ($r = 0.63$, p-smash < 0.001, scatter plot in Fig. 2a) and a weaker correlation with DC ($r = 0.31$, p-smash = 0.01, Fig. 2b). The group surface and graph plots in Fig. 2 illustrate the varying distribution of hub regions for MwC and DC. While MwC hubs are located in medial and lateral parietal and lateral frontal regions, DC hubs occur mainly in sensory-motor regions (see Supplementary Fig. S1 for additional details). The stronger association of the fully-weighted MwC compared to edge-oriented DC in relation to CMRglc is also evident at the subject level, as shown in the violin plots of Fig. 2. MwC values range from $r = 0.30 - 0.62$ (all $p < 0.05$), while the DC values range from $r = 0.10 - 0.27$ (for significant cases only).

Finally, we performed identical analyses on the two independent replication datasets and observed similarly strong ($r = 0.51 – 0.57$) correlations for MwC with CMRglc (see Supplementary Fig. S2). In addition to DC, we also tested another prominent edge-oriented centrality measure, participation coefficient (PC), to explain signaling-related energy metabolism. Similarly to DC, PC showed a weaker correlation with CMRglc ($r = 0.29$, $p = 0.03$) than MwC (see Supplementary Fig. S3).

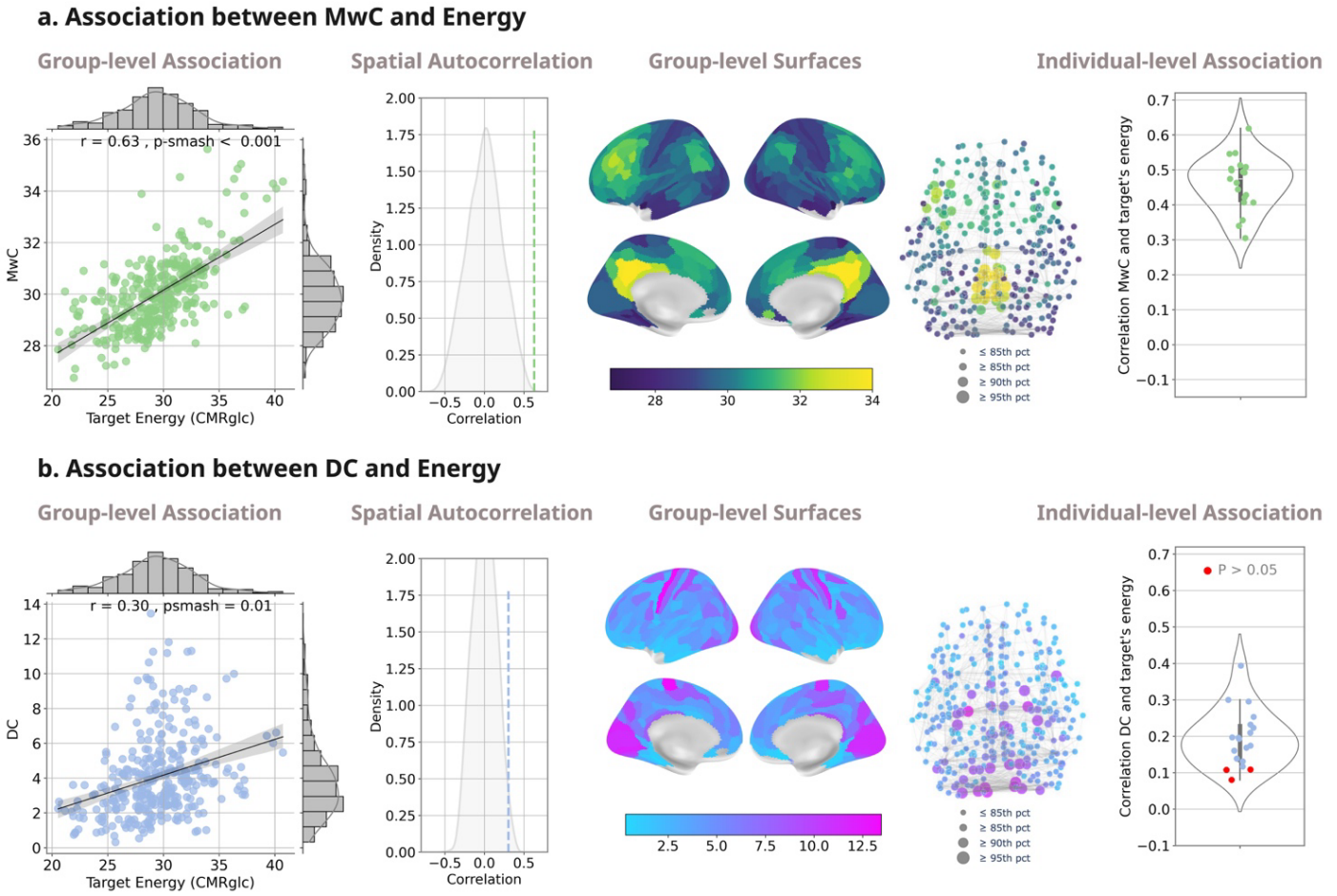

Fig 1: Comparison between MwC and DC in describing regional energy metabolism. (a) Association between MwC and CMRglc at the group and individual subject levels. The linear regression plot shows the significant association between calculated MwC and measured CMRglc of target regions across the cortex at the group level. The histogram plot illustrates the null distribution, derived from Brainsmash, while the dashed line represents the empirical correlation, which assesses the influence of spatial autocorrelation. The empirical correlation (dashed line, r = 0.63) lies outside the 90th percentiles (r = $\pm$ 0.31) of the null distribution. The four brain surfaces illustrate the group-level MwC values, with lower values in dark blue and higher values in yellow. The graph plot representation highlights regions with the highest values (≥85th, ≥90th, and ≥95th percentiles), shown as progressively larger node sizes, and color coding is consistent with the group-level surface maps. The violin plot shows the significant subject-level correlations, where each dot represents the individual correlation between regional MwC and CMRglc. **(b)** Association between DC and CMRglc at the group and individual subject levels. The linear regression plot reveals a moderate correlation between regional DC and CMRglc across all brain regions. The histogram plot illustrates the empirical correlation (dashed line, r = 0.31) against a null distribution corrected for spatial autocorrelation (90th percentile r = $\pm$ 0.26). The brain surfaces illustrate the group-level DC values across cortical brain regions. The graph plot representation highlights the top 5%, 15%, and 25% of regions with the highest DC values, represented as increasing node sizes, while maintaining the same color coding as in the group-level surface plots. The violin plot details subject-level correlations, with red dots highlighting nonsignificant correlations.

Additionally, we performed several control analyses. First, we tested the statistical difference between MwC and DC regarding their correlation with CMRglc. Across the joint results from all

three datasets (Supplementary Fig. S4), MwC was significantly stronger correlated with CMRglc than DC (Steiger's test, Z = 2.54, p = 0.01). A stepwise, multiple linear regression revealed that MwC explained 39.9% of CMRglc variance, while DC additionally explained 4.2% of variance in energy metabolism. Second, we assessed the relevance of each component in the two-layer network to the sensitivity of the MwC calculation. Removing the E(i) term – thereby reducing MwC to DC – lowered the group-level correlation from 0.63 to 0.31 ($p < 0.001$), with individual correlations dropping to 0.10 – 0.27 (all $p < 0.05$). Removing the effect of nFC for each target by replacing it with identical weights across all connections resulted in a similar reduction in performance (group-level r = 0.33, $p < 0.001$; individual r = 0.11 – 0.52). Third, we tested whether the true matching of regional connectivity and metabolism is necessary, or whether the mere scaling of DC with arbitrary metabolism is sufficient to explain our finding. To do this, we shuffled the connection weights across the vector of regional energy values. This preserved the regional distribution of energy metabolism and the pattern of brain-wide connectivity but disrupted their true pairing. Across 500 iterations, the correlation values between MwC and CMRglc dropped to around zero, both on the group- and subject-level (Supplementary Fig. S5a). This analysis demonstrates that merely including metabolic data is not sufficient to explain the observed correlation with CMRglc. Finally, several sensitivity analyses confirmed that the observed MwC-CMRglc correlations were stable across different thresholding levels and were unaffected by region size (Supplementary Fig. S5b).

MwC is a robust measure of network organization and cognitive processing

In the following section, we investigated the distribution of MwC across large-scale brain networks and whether MwC indicates the complexity of cognitive domains processed by cortical regions.

Fig. 3a shows the group average regional values of MwC (upper graph) and DC (lower graph), color-coded according to six major functional brain networks (Yeo et al., 2011) and sorted in ascending order based on the networks' medians. Our findings reveal that MwC significantly increases from sensory (visual, VIS; sensory-motor, SOM) to higher cognitive networks, including the default mode network (DMN), salience/ventral attention (SAL), and control network (CON) (One-way ANOVA, F = 31.36, p-value < 0.001; post-hoc Tukey test: $p<0.05$). In contrast, the average DC showed a less distinctive distribution across all networks (F = 2.97, p-value = 0.01). Significant pairwise differences between mean network centrality measures are marked with colored stars, and these were more prevalent in MwC compared to DC.

We then evaluated the diversity of regional network connectivity. For each region, we calculated the Simpson Diversity Index (SDI), which indicates whether a region mainly connects with its own network (SDI close to 0) or with multiple networks (SDI close to 1). Our analysis revealed a significant positive correlation between SDI and MwC, and to a lesser extent, with DC (Fig. 3b).

Finally, we compared the regional distribution of MwC and DC with the distribution of regional activity related to major cognitive functions, as identified in the Neurosynth database (Margulies et al., 2016). We extracted the activity patterns of 24 major cognitive domains and ranked their correlations with MwC (upper section) and DC (lower section) in the circular diagrams of Figure 3c. Notably, MwC effectively distinguishes between higher cognitive (represented in orange, such as inhibition and memory) and sensory-motor processing (represented in blue). In contrast, DC

did not clearly differentiate between these two categories; for example, tasks related to "visuospatial" and "eye movements" were more associated with regions of higher DC values rather than lower values.

In summary, MwC serves as a robust and distinctive measure of brain network organization and its relationship with cognitive processing, complementing edge-oriented approaches with specific information about signaling hubs within the brain's connectome.

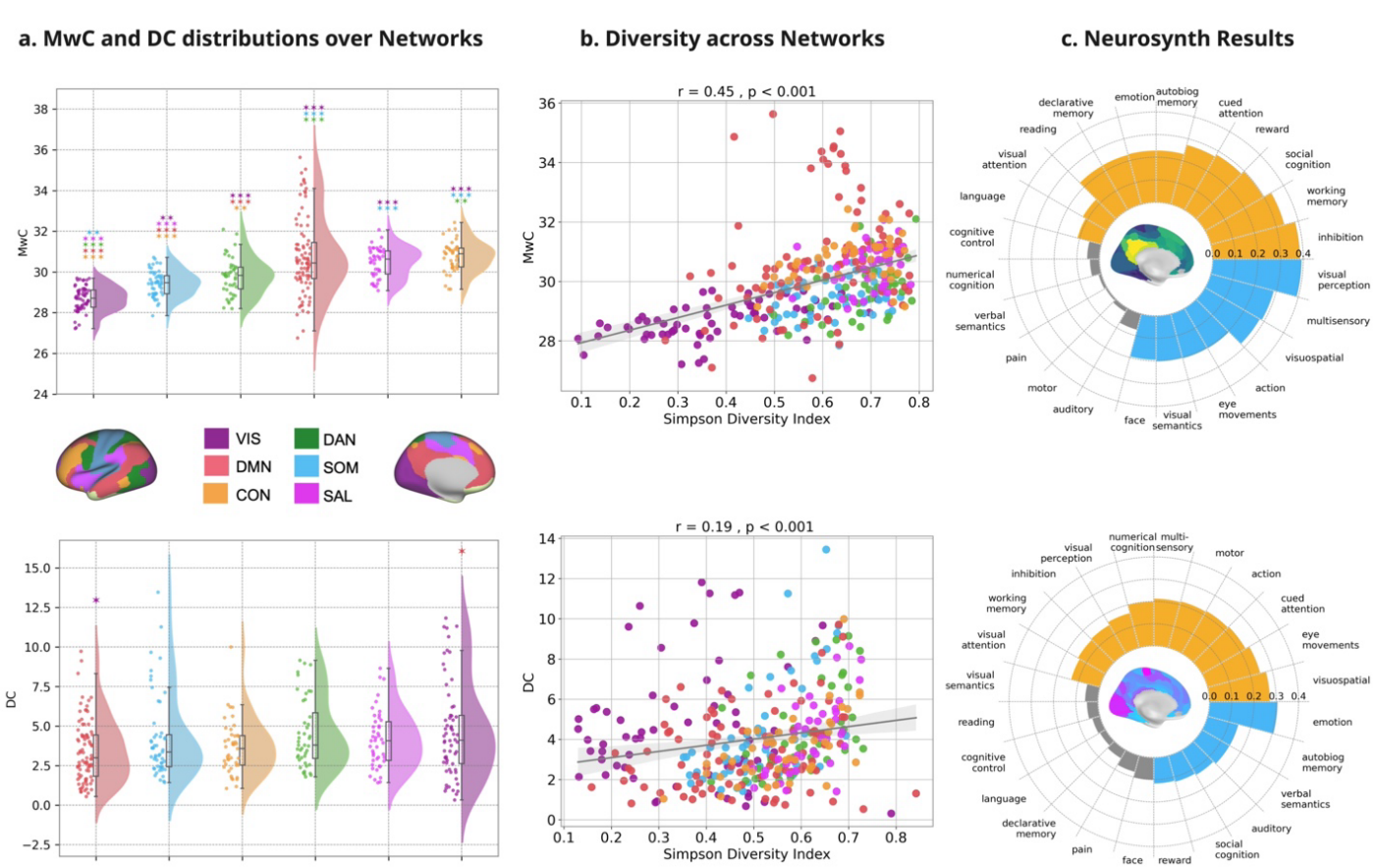

Fig 3: Brain network and cognitive domain mapping. (a) MwC and DC distribution across macroscale brain networks. Brain regions are sorted by functional brain networks (Yeo et al., 2011). The top row shows the group-level MwC, whereas the bottom row shows the DC distribution. The brain surfaces illustrate the distribution of six Yeo-networks across the cortex. Both MwC and DC are ordered in ascending order of median network values. Colored stars indicate significant differences between each pair of networks based on post hoc comparisons (Tukey's HSD test following one-way ANOVA, * ≡ $p<0.05$, ** ≡ $p<0.01$, *** ≡ $p<0.001$). Different colors of stars correspond to pairwise comparisons of each network with the others, each color representing a specific network. **(b)** Information Diversity of Networks. Simpson's diversity index indicates the connectivity diversity of brain regions across networks. The upper scatter plot shows a significant positive correlation between MwC and SDI. DC is less significantly correlated with SDI (lower). **(c)** Cognitive domain mapping. Circular diagrams show correlation values between 24 Neurosynth categories and MwC (upper) and DC (lower). Orange sectors represent significant positive, and blue sectors negative correlations, while gray sectors indicate nonsignificant correlations. MwC is consistently and significantly correlated with higher cognitive tasks (e.g., inhibition, memory, cognition, attention) and negatively correlated with sensory-motor tasks (e.g., visual, motor). This distinction is less consistent for DC.

MwC is linked to signaling, metabolic pathways and neurodegenerative diseases

In the final section, we investigated the biological plausibility of the MwC metric. First, we tested whether independently sampled transcriptomics data confirm the regional levels of signaling activity and metabolism as indicated by the measure of MwC. We mapped gene expression data from the Allen Human Brain Atlas (AHBA) (Hawrylycz et al., 2012) onto the HCP MMP-atlas and used partial least squares (PLS) regression to identify genes significantly expressed in relation to MwC. At the group level, we found a positive correlation ($r = 0.51$, $p < 0.001$) between the first PLS component of genes (PLS1) and MwC (Fig. 4a). A subsequent gene enrichment analysis of PLS1-genes with positive Z-scores revealed two major gene clusters that were significantly over-represented in regions of high MwC: genes associated with metabolic activity and synaptic signaling (Fig. 4b). Among the metabolic genes, significant clusters were related to 'mitochondrial membrane', 'transporter complex' and 'mitochondrial matrix'. The majority of significant gene clusters related to synaptic signaling included compartments such as 'presynapse', 'postsynapse', or the 'dendritic tree' (see Table 1 in the supplementary for detailed information on each cluster). Control analyses using randomly selected genes confirmed the specificity of these associations (Fig. S6).

Following the transcriptomics analysis results, we explored independent imaging data on synaptic and mitochondrial density in the human brain to evaluate their relationship with MwC. The brain surfaces in Fig. 4c illustrate group-average data of [^{11}C]UCB-J PET imaging of the synaptic vesicle glycoprotein 2A (SV2A), which serves as a marker of synaptic density (Johansen et al., 2024). We found a significant positive correlation between synaptic density and MwC across the cortex ($r = 0.33$, $p < 0.001$). We also studied the relationship between MwC and mitochondrial density (MitoD) as well as mitochondrial respiratory capacity (MRC) (Mosharov et al., 2025), but did not find any significant correlation (see Supplementary Fig. S7).

Finally, we used the KEGG database to identify biological and pathological pathways related to the genes of the PLS1. KEGG analysis revealed "oxidative phosphorylation" as the most significant pathway. Among the nine additional significant pathways identified, six were associated with neurodegenerative diseases (Fig. 4d, bar plot). This suggests that high MwC regions are not only metabolically active but also particularly vulnerable to neurodegeneration. To further validate this finding, we used an external dataset of amyloid-PET imaging, which visualizes amyloid plaques - a hallmark of Alzheimer's Disease – to determine if high MwC regions are especially prone to the accumulation of amyloid plaques. Consistent with the KEGG analysis results, we found a significant positive correlation between MwC and amyloid load in both cognitively normal ($r = 0.32$, $p < 0.001$) and amyloid-β-positive (Ab.pos) MCI patients ($r = 0.4$, $p < 0.001$), an early stage of Alzheimer's disease (Fig. 4d, regression plots).
In summary, both gene and imaging data indicate that MwC hubs exhibit high signaling capacity and metabolic activity. However, these regions also demonstrate heightened susceptibility to neurodegenerative processes, underscoring the potential of MwC as a crucial metric for understanding the molecular underpinnings of brain health and dysfunction.

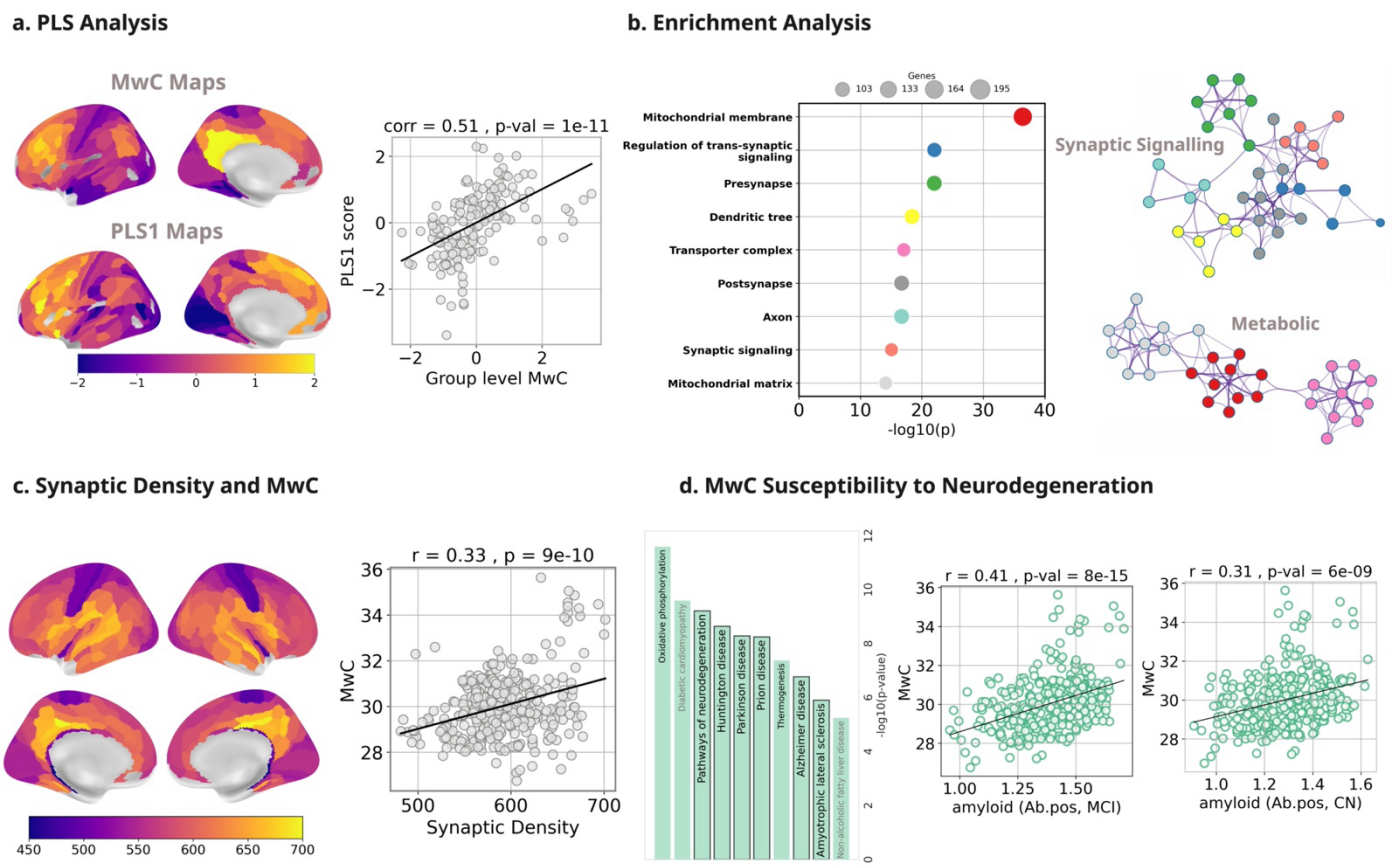

Fig 4: Biological plausibility analyses of MwC. (a) Partial least squares (PLS) analysis was performed to link MwC to gene expression data from the Allen Human Brain Atlas (AHBA), using MwC as the response variable and regional gene expression as regressors. Brain maps display group-level MwC and the first principal component of PLS (PLS1), with a positive correlation between MwC and PLS1 in the scatter plot. **(b)** Gene enrichment analysis for positive Z-score genes using Metascape (Zhou et al., 2019) highlights clusters with shared characteristics, visualized in the left diagram. Clusters with p <1e-10 are shown, with marker size denoting gene counts. The mitochondrial membrane cluster (red) has the most genes and the smallest p-value, emphasizing its significance. The top subnetwork relates to synaptic signaling (e.g., colored clusters for synapses, axons, dendrites), while the bottom predominantly features metabolic clusters**. (c)** Relationship between synaptic density and MwC. Surface maps show regional synaptic density based on SV2A PET imaging ([11C]UCB-J). Warmer colors indicate higher synaptic density. The scatter plot shows a significant positive correlation between synaptic density and MwC across regions (r = 0.33, p = 1e-09), suggesting that regions with higher synaptic density tend to have higher MwC values. **(d)** KEGG pathway enrichment analysis for positive PLS1 Z-score genes identifies the top 10 significant pathways. Brain-related pathways are printed in black, while neurodegenerative disease pathways are emphasized with bold black outlines. Scatter plots illustrate the association between MwC and independent, beta-amyloid imaging data for MCI patients (left) and cognitively normal (CN) subjects (right), revealing a significant positive correlation in each.

Discussion

Brain graphs are common tools to characterize the signaling architecture of the brain. Traditionally, the graph topology is defined by the degree and strength of edges derived from functional or structural connectivity data. However, the level of signaling activity within individual nodes has not been considered so far. We extend this approach by incorporating node-specific metabolic activity, scaling edge weights in proportion to the signaling-related metabolic demands of connected regions. As a result, we create a fully weighted brain graph that introduces MwC as a novel measure of nodal signaling dominance within the entire network. MwC reflects the metabolic effort a region expends on information processing and integration across its network connections. Our findings indicate that connections with equal FC strength may contribute differently to information processing depending on the metabolic activity in connected regions. Unlike hubs identified from FC or SC data, which are highly connected in a topological sense, MwC hubs are regions that engage in metabolically demanding communication and serve as active signaling hubs. We validated MwC using transcriptomic data and imaging data on synaptic density, demonstrating its biological relevance. Importantly, regions with high MwC values overlap with areas known to be vulnerable in various neurodegenerative disorders, suggesting that metabolic load may underlie susceptibility to neurodegeneration. This shifts the interpretation of hubness from a purely topological concept that describes only the presence of pathways to one motivated by signaling activity, offering a more biologically plausible perspective on the brain's functional connectome.

Energy metabolism is a well-established indicator of signaling activity (Attwell & Laughlin, 2001; Harris et al., 2012; Karbowski, 2012; Hyder et al., 2013). Therefore, any interpretation of connectivity strength as a measure of information transfer or integration should align with the metabolic demands of regions involved. Previous research, including our own, has demonstrated that edge-oriented centrality of nodes correlates with their energy metabolism to some extent (Castrillon et al., 2023; Aiello et al., 2015). In the present study, we found that MwC and DC together explain approximately 44% of the variance in CMRglc, with MwC accounting for the majority of the variance. This finding underscores the importance of understanding the signaling activity in each connected node; relying solely on DC or metabolism for a given region captures only a part of its signaling dominance. This is supported by work showing how microscale data of cellular composition vary across macroscale regions (Scholtens et al., 2022; X.-H. Zhang et al., 2024; Howarth et al., 2020). By considering edge information in conjunction with nodal signaling activity, we achieve a more biologically accurate representation of an activity-driven connectome architecture.

Both FC and SC, derived from human MRI, primarily capture the presence of a connection rather than the level of signaling along it. In FC graphs, an edge between two regions is identified when their fluctuations of the BOLD signal time series are synchronized. Higher synchrony indicates a strong shared component in the signal dynamics of both regions, but does not necessarily reflect high signaling throughput. Critically, BOLD signal fluctuations represent only a small portion of the total activity occurring in a region (Hoge & Pike, 2001; Hyder & Rothman, 2010). In other words, the amplitude or dynamics of signal fluctuations are independent of the absolute level of

activity, which fMRI is unable to measure. Moreover, different hemodynamic mechanisms contribute to the BOLD signal (Drew, 2022), and our recent work has shown that changes in BOLD signal amplitude do not reliably indicate metabolic changes (Epp et al., 2023). This leads to crucial limitations in fMRI-based FC: two regions with low overall activity can appear strongly connected if their BOLD fluctuations are highly similar. In such cases, centrality metrics may mistakenly identify a region as a hub – not due to its active role in information processing, but rather because of its synchronous low-level activity with other regions (Bijsterbosch et al., 2020). This issue becomes particularly relevant when a temporal component contributing to the synchrony is shared by many regions, resulting in the appearance of a hub, even if there isn't a substantial level of signaling among all connected regions (Peterson et al., 2025; Van Den Heuvel & Sporns, 2013). Thus, relying on FC alone cannot provide a true measure of the signaling occurring along the edges, a limitation that MwC addresses by scaling edges according to the absolute metabolic demand of each region.

Numerous brain imaging studies have aimed to identify hubs within the connectome using various centrality measures such as degree centrality, betweenness centrality, and eigenvector centrality (Buckner et al., 2009; Cole et al., 2010; Liao et al., 2013; Van Den Heuvel & Sporns, 2013; Nijhuis et al., 2013; Hagmann et al., 2008). More advanced metrics like PC (Power et al., 2013) and entropy-based indices (Wang et al., 2022) have also been utilized. These methods primarily rely on edge-oriented graphs, with DC and PC being particularly popular indicators of hubs. However, identifying hubs in graphs is sensitive to multiple factors, including the imaging modality, preprocessing pipeline (Tomasi & Volkow, 2011; Smith et al., 2023; Gajwani et al., 2023; Liu et al., 2025), and the resolution of the graph. For example, voxel-level connectomes often yield different hub maps compared to region-level connectomes (Smith et al., 2023; Cole et al., 2010; Zuo et al., 2012; Zamani Esfahlani et al., 2020). Additionally, as noted by Power et al. (2013), correlation-based metrics are influenced by module size and internal coherence. This means that a region within a large, tightly interconnected module may appear central due to its structural position, rather than its functional role. Thus, merely having numerous connections does not necessarily indicate functional importance, and other parameters might be more relevant (Del Ferraro et al., 2018). While variations of graph metrics exist, they still rely on the same fundamental edge data (Faskowitz et al., 2020). Other researchers have also recognized the importance of node characteristics such as neurotransmitter distribution (Murphy et al., 2016; Bassett & Sporns, 2017; Bazinet et al., 2023; Hansen et al., 2023; Shine et al., 2019) However, in these cases, nodal information primarily serves as a template for selecting subgraphs, while hubness and DC were still calculated solely based on BOLD signal coherence. In contrast to edge-oriented calculations, our node-weighted approach integrates both measures effectively. We showed that MwC more distinctly segregates along functional networks and reflects differences in signaling and cognitive roles compared to DC (Fig. 3). Specifically, high-MwC hubs represent regions with greater signaling complexity and processing capacity, while high-DC hubs tend to be more diffusely distributed across networks, often emphasizing structural prominence rather than metabolic load.

Finally, our results are supported by independent data from molecular imaging and transcriptomics. Gene enrichment analysis revealed that MwC hubs have significantly

upregulated genetic pathways related to synaptic signaling and mitochondrial function. Additionally, imaging data from SV2A PET revealed a higher synaptic density in MwC hubs. This indicates that the high integration capacity of MwC hubs is supported by their dense synaptic and metabolic infrastructure. Still, the transcriptional upregulation of mitochondrial genes did not match the mitochondrial density map, possibly due to the limited brain coverage and generalizability of the single-subject data of the map. Finally, we found a higher accumulation of amyloid-β in MwC hubs. This suggests that regions with high lifelong signaling and metabolic turnover may be particularly vulnerable to Alzheimer's pathology (Bobba-Alves et al., 2023; Morella et al., 2022; Sercel et al., 2024; Watts et al., 2018). In summary, MwC identifies brain regions of strong signaling dominance and integration within the entire brain connectome, highlighting the susceptibility of highly active network nodes to neurodegeneration.

Materials and Methods

Participants

Our analysis incorporates three independent datasets for main results (TUM.main) and replication analyses (TUM.rep, Vienna.rep). All participants were right-handed and did not have any documented psychiatric conditions. Before data collection, participants provided informed consent and were apprised of potential risks. Data acquisitions were conducted with approval from the ethics committees at Klinikum Rechts der Isar, Technische Universität München, and the Medical University of Vienna. The TUM.main dataset included twenty participants, evenly divided between genders, with an average age of 34.45 ± 5 years. The TUM.rep dataset comprised ten subjects with an average age of 27 ± 5, also equally split between genders. The Vienna dataset consisted of five males and five females, with an average age of 27 ± 7 years. For the TUM.main and Vienna datasets, participants kept their eyes open, while participants in the TUM.rep dataset had their eyes closed during resting state data acquisition.

Data acquisition

Both TUM datasets were acquired on an integrated 3T PET/MR Siemens Biograph scanner with a 12-channel head coil for MRI imaging. PET data were gathered in list-mode format with an average intravenous bolus injection of 184 MBq (s.d. = 12 MBq) of [18F]FDG. Concurrently, every second, automatic arterial blood samples were taken from the radial artery to measure blood radioactivity using a Twilite blood sampler (Swisstrace, Zurich, Switzerland). Functional MRI data were acquired over a 10-minute interval using a single-shot echo planar imaging sequence (300 volumes; 35 slices; repetition time, TR = 2000 ms; echo time, TE = 30 ms; flip angle, FA = 90°; field of view, FOV = 192 × 192 mm2; matrix size = 64 × 64; voxel size = 3 × 3 × 3.6 mm3). Diffusion-weighted images (DWI) were acquired with a single-shot echo planar imaging sequence (60 slices; 30 non-colinear gradient directions; b-value = 800 s/mm2 and one b=0 s/mm2 image; TR = 10800 ms, TE = 82 ms; FA = 90°; FOV = 260 × 264 mm2; matrix size = 130 x 132; voxel size = 2 × 2 × 2 mm3). Anatomical images were based on a T1-weighted 3D-MPRAGE sequence (256 slices; TR = 2300 ms; TE = 2.98 ms; FA = 9°; FOV = 256 × 240 mm2; matrix size = 256 × 240; voxel size = 1 × 1 × 1 mm3). We used the same data as Castrillon 2023; for details on the data acquisition and preprocessing, see this paper.
The data acquisition from the Vienna site followed similar protocols to those used at the TUM site, as previously detailed by Sundar et al. 2019. Key differences included a higher and more variable dose of injected [18F]FDG (mean dose = 356 MBq, SD = 66 MBq), the manual measurement of blood radioactivity for the arterial input function, and slight adjustments in the fMRI protocol, such as a shorter acquisition time (~7 min), a repetition time (TR) of 2400 ms, and a voxel size of 2 × 2 × 3.7 mm^3.

MRI processing

The structural and functional MRI data preprocessing was conducted using the Configurable Pipeline for the Analysis of Connectomes (C-PAC, version 1.4.0) following established procedures:

- Anatomical images underwent skull-stripping, segmentation into the cerebrospinal fluid (CSF), white matter (WM), and gray matter (GM), and were registered to the MNI152NLin6ASym template. Individual GM masks were generated based on probability thresholds and temporal signal-to-noise ratios.
- Functional image processing included slice-time correction, realignment, motion correction, skull-stripping, and registration to anatomical images. Global mean intensity was normalized, nuisance signals (scanner drift, physiological noise, head motion) were regressed out, and time series were bandpass filtered.

DWI preprocessing and probabilistic tractography were executed using MRtrix3 (Tournier et al., 2019), FSL, and Advanced Normalization Tools (ANTs), incorporating denoising, eddy-current correction, motion correction (using FSL top-up), and bias-field correction (using ANTs). Structural connectivity (SC) matrices were derived via constrained spherical deconvolution probabilistic tractography. Spherical-deconvolution-informed filtering was applied to pictograms constrained by anatomical tissue masks and the HCP-MMP parcellation. The strength of SC was assessed based on communicability between brain regions, encompassing both direct and indirect connections.

PET processing

PET imaging data acquisition for both TUM datasets involved offline reconstruction of the initial 45-minute period using the NiftyPET library (Markiewicz et al., 2018). This reconstruction employed the ordered subsets expectation maximization (OSEM) algorithm with 14 subsets and 4 iterations divided into 33 dynamic frames. These frames consisted of 10 intervals of 12 seconds, 8 intervals of 30 seconds, 8 intervals of 60 seconds, 2 intervals of 180 seconds, and 5 intervals of 300 seconds. Attenuation correction relied on T1-derived pseudo-CT images (Burgos et al., 2014). All reconstructed PET images underwent motion correction and spatial smoothing using a Gaussian filter with a full width at half maximum (FWHM) of 6 mm. The net uptake rate constant (Ki) was determined using the Patlak plot model (Patlak & Blasberg, 1985) based on the last 5 frames of the preprocessed PET images (frames occurring between 20 to 45 minutes) and the arterial input function derived from preprocessed arterial blood samples. The cerebral metabolic rate of glucose (CMRglc) was computed by multiplying the K_i map with the concentration of glucose in the plasma of each participant, divided by a lumped constant of 0.65 (Wu, 2003). Finally, the CMRglc maps underwent partial volume correction using GM, WM, and CSF masks derived from the T1 images via the iterative Yang method (Yang et al., 2017). They were registered to the MNI152NLin6ASym 3 mm template through the anatomical image.

Model description

The MwC model involves two main steps: (1) constructing a fully-weighted graph and (2) calculating the MwC for each brain region.

1. Construction of a fully-weighted graph

All analyses were performed at the regional level using 334 cortical regions from the Human Connectome Project Multi-Modal Parcellation (HCP-MMP) atlas (Glasser et al., 2016). Regions from the limbic network were excluded due to instability in CMRglc values (see Fig. S8).
Each region's mean BOLD time series was calculated and used to compute pairwise FC via mutual information (MI). MI quantifies the statistical dependence between two regions' time series *X* and *Y*, capturing both linear and nonlinear relationships. We used Gaussian Copula Mutual Information (GCMI) (Ince et al., 2017) to estimate MI efficiently, assuming continuous variables transformed to a standard normal distribution. MI was computed as:

$$MI(X,Y) = \int_x \int_y \mathrm{p}(x,y) log_2(\frac{p(x,y)}{\mathrm{p}(x)p(y)})\, dx\, dy. \quad (1)$$

p(x,y) is the joint probability density of two arbitrary regions' time series *X* and *Y*, while *p(x)* and *p(y)* are their marginal densities.
SC was obtained from probabilistic tractography using MRtrix3-based on diffusion-weighted imaging. We applied proportional thresholding to retain the top 10% of SC values and binarized the resulting matrix to define the presence or absence of structural connections.
The fully-weighted brain graph was constructed by combining structural, functional, and metabolic information:

- **Edges** were assigned weights equal to the MI between functionally connected regions, but only if a structural connection (from the binarized SC matrix) was present. This was implemented by element-wise multiplication of the SC and MI matrices, resulting FC matrix.
- **Nodes** were annotated with metabolic activity values *E*, defined as the regional median of the CMRglc from FDG-PET data.

This graph forms the basis for calculating the MwC, integrating both regional energy metabolism and the structure-function topology of the connectome.

2. Metabolism-weighted Centrality (MwC)

For each target region *t*, defined as any node for which the metric is computed, the MwC was calculated based on the normalized functional connectivity (nFC) to its connected neighbors and their corresponding metabolic activity.
Let $i \in \{1,2,...,N\}$ denote the *N* regions connected to region *t*. The FC between *t* and *i*, denoted *FC(t,i)* was calculated using MI and SC matrices. The metabolic activity of region *i*, *E(i)*, corresponds to its median CMRglc, derived from FDG-PET.
To control for the effect of connection count and total FC strength on MwC, we normalized the FC values for each target region as follows:

$$nFC(t,i) = \frac{FC(\mathrm{t,i})}{M} \quad (2)$$

$$M = \sum_{i=1}^{N} FC(t,i) \quad (3)$$

This normalization ensures that:

$$\sum_{i=1}^{N} nFC(t,i) = 1 \quad (4)$$

and that the contributions of neighboring nodes are interpreted as proportions rather than absolute values. This prevents target regions with more or stronger raw FC values from yielding artificially inflated MwC scores. Using these normalized weights, MwC was defined as the weighted sum of the metabolic activity of the connected neighbors:

$$MwC(t) = \sum_{i=1}^{N} nFC(t,i) \times E(i) \quad (5)$$

By this definition, MwC is high when a target region is connected to neighbors that have both high metabolic activity *E(i)* and high normalized FC values *nFC(t,i)*. Conversely, MwC is low when neighbors have low metabolic activity and low nFC weights. The CMRglc of the target region itself is excluded from the calculation, avoiding direct dependence between the predictor and outcome in correlation analyses.

Degree Centrality (DC)

DC was calculated using a conventional edge-weighted graph based solely on FC. First, we found the Pearson correlation between mean BOLD time series of region pairs, consistent with prior studies that have commonly used this approach. The resulting matrix was proportionally thresholded at 20% and then masked using a binarized SC matrix (top 10%) to retain only anatomically plausible connections. We call the final matrix as the FC matrix. For each target region *t*, DC was computed as:

$$DC(t) = \sum_{i=1}^{N} FC(t,i) \quad (6)$$

where *N* is the number of connected neighbors and *FC(t,i)* is the connection strength between nodes *t* and *i*.

Participation Coefficient (PC)

PC was calculated to quantify the extent to which each region distributed its connections across different modules. We used the same structurally constrained and thresholded FC matrix as in DC analysis. Community structure was identified using the Infomap algorithm (Rosvall & Bergstrom, 2008), as previously applied in brain networks by by Power et al. 2011, 2013. Then, the Infomap algorithm was applied to the FC matrix for each subject. For a given target region *t*, PC was defined as:

$$PC(t) = 1 - \sum_{m=1}^{M} \left(\frac{k_{t,m}}{k_t}\right)^2 \quad (7)$$

where *M* is the total number of detected modules, $k_{t,m}$ is the sum of FC weights between region *t* and all regions in module *m*, and k_t is the total degree of region *t*.
Then regional PC values were averaged across subjects for group-level analysis. Their association with regional CMRglc was evaluated using spatial autocorrelation-corrected permutation testing (Brainsmash).

Control analyses

To evaluate the contribution of each model component, we systematically deleted the effect of each component from the MwC definition and generated a surrogate MwC, then we found the relation between the MwC_{sur} and CMRglc.

First, we removed the metabolic term *E(i)*, reducing the model to:

$$MCC_{sur}(t) = \sum_{i=1}^{N} nFC(t,i) \tag{8}$$

which is equal to one based on equation 4 for all nodes and is therefore uninformative. To create meaningful surrogate data, we instead used raw FC values, which makes MwC similar to the DC definition in equation 6, with one main difference: here, we have an MI-based FC matrix.

Then, we generated surrogate data by excluding the contribution of nFC data and preserving the same $E(i)$ values as in the actual data. We manipulated the *nFC* values by assigning equal values to all connections, such that each connection's strength is set to $1/N$ if a target has *N* connected regions, since the sum of all connected regions' nFC values is equal to one (equation 4):

$$MCC_{sur}(t) = \frac{1}{N}\sum_{i=1}^{N} E(i) \tag{9}$$

This version corresponds to the average CMRglc of connected neighbors and removes the influence of varying FC strength.

For both surrogate metrics, we computed their correlation with regional CMRglc to assess the effect of removing or flattening each component.

To test whether the observed MwC–CMRglc association depends on the specific alignment between FC weights and neighboring metabolic values, we performed a permutation-based analysis. For each region, we preserved the set of connected neighbors and their CMRglc values but randomly reassigned the FC weights across them. Specifically, for each region *t*, the values *FC(t,i)* were randomly shuffled across the set *i=1,...,N*, MwC was then recomputed as:

$$MCC_{sur}(t) = \sum_{i=1}^{N} nFC^{shuffled}(t,i) \times E(i) \tag{10}$$

This procedure was repeated 500 times per subject. For each iteration, we computed the correlation between MwC_{sur} and true CMRglc. The resulting distribution served as a null model (Fig. S5a).

As the second part of the control analysis, we conducted a sensitivity analysis by altering specific variables and monitoring their effect on the main result, the correlation between MwC and the target's energy. We analyzed three variables: the SC threshold, the MI threshold, and the target region size. We explored different threshold levels for the first two variables to assess their effect on the correlation between MwC and CMRglc at the group level. We defined the target size as the number of voxels within each target region.

Statistical analyses

All statistical analyses were conducted at the regional level. We used Pearson correlation to assess the association between each metric and the regional cerebral metabolic rate of glucose (CMRglc), both at the group level (after averaging across subjects) and at the individual level.
To evaluate the statistical significance of spatial correlations while accounting for spatial autocorrelation, we used Brainsmash (Burt et al., 2020), which generates null brain maps that preserve the spatial autocorrelation structure of the empirical data. For each test, we generated 1.000 spatially autocorrelated surrogate maps of CMRglc and calculated their correlation with the metric of interest. A two-sided p-value was computed based on the rank of the observed correlation within the null distribution.
To assess differences across networks in Fig. 3a, we first conducted a one-way ANOVA to test for overall significant differences. Then, to see the pairwise differences among networks, the post hoc Tukey's HSD (Honestly Significant Difference) test compared the means of each network.
To determine whether the relationship with CMRglc significantly differed between MwC and DC, we applied Steiger's Z-test for dependent correlations (Steiger, 1980). This test compares two correlation coefficients that share a common variable (CMRglc) within the same dataset. To ensure adequate statistical power for this test, we combined the z-scored values from our three datasets, resulting in a total sample size of 45. Finally, we evaluated the unique and shared contributions of MwC and DC in explaining variability in CMRglc using linear regression analysis. We implemented two models: one including only MwC as a predictor (CMRglc ~ MwC), and another including MwC and DC as predictors (CMRglc ~ MwC + DC). This approach allowed us to quantify the additional variance explained by DC beyond what is captured by MwC alone.

Simpson Diversity Index (SDI)

SDI, also known as the Gini-Simpson Index, quantifies diversity by measuring the probability that two entities randomly selected from a dataset belong to the same type (Simpson, 1949). Mathematically, it is defined as:

$$SDI = 1 - \sum_{i=1}^{S} p_i^2 \tag{11}$$

In this context, S represents the total number of networks, which amounts to 6 distinct networks. The symbol p_i denotes the proportional abundance of each network i. We individually calculated the diversity of *SDI* for each target region. The goal was to quantify the diversity of networks within the connected regions. For a specific target region, p_i indicates the number of connected regions that belong to network type i, relative to the total number of connections. The *SDI* index ranges from 0 to 1: a value of 0 indicates no diversity (meaning all entities are of a single type), while a value of 1 denotes maximal diversity, where each network type is equally represented.

Neurosynth analysis

Neurosynth is a platform that automates the large-scale synthesis of fMRI data (Yarkoni et al., 2011). It utilizes a database of thousands of published fMRI studies to generate meta-analytic maps based on frequently recurring key terms. This innovative tool enables an objective and

quantitative exploration of brain activity associated with various cognitive and sensory processes. Our analysis, particularly in Fig. 3, used brain maps for 24 cognitive topic terms drawn from previous studies (Margulies et al., 2016; Preti & Van De Ville, 2019). These topics range from lower sensory and motor functions to higher cognitive functions. We examined the correlation between each of these 24 maps and the group-level MwC and DC maps to explore the cognitive implications of each metric.

Gene expression analysis using AHBA data

We analyzed regional gene expression levels for 15,631 genes from transcriptomic measurements in six postmortem brains from six donors, as provided by the Allen Human Brain Atlas (AHBA) (Hawrylycz et al., 2012). Using the Abagen toolbox (Markello et al., 2021), the data was mapped to cortical regions according to the multimodal parcellation (MMP) atlas. Our analysis focused on the left hemisphere due to the availability of complete data for this hemisphere in some donors.

Partial Least Squares (PLS)

We used PLS regression to examine the relationship between the group-level MwC map and the gene expression maps of 15631 genes across 180 regions in the left hemisphere, derived from the AHBA microarray measurements. The expression levels of these genes were represented in a 180 x 15631 matrix, serving as the predictor variables. In contrast, the group-level MwC map was represented as a 180 x 1 vector, acting as the response variable. The first PLS component (PLS1) reflects the cortical expression map most closely associated with the MwC. We implemented permutation testing to evaluate the statistical significance of the variance explained by this PLS component, performing 1,000 iterations. Additionally, we used a bootstrapping procedure to assess the contribution of each gene to PLS1. We calculated the Z score for each gene by taking the ratio of its weight to its bootstrap standard error and then ranked the genes based on their contributions to PLS1 (Morgan et al., 2019).

Gene enrichment analysis

We used the Metascape (http://metascape.org) (Zhou et al., 2019), an automated meta-analysis tool, for our gene enrichment analysis. We input the genes exhibiting positive z-score values from the first PLS component into the Metascape website. We tested whether the input gene list shared enrichment pathways with GO “Molecular Functions”, “Biological Processes”, and “Cellular Components” pathways. We used the default parameters on the Metascape website. Metascape’s input limit is 3000 genes; we selected the top 3000 genes with positive Z score values for our analysis. Within the Metascape results illustration, pathways are ordered based on their p-value. We included the connected clusters and removed the small, isolated clusters.
We also did the enrichment analysis for the KEGG 2021 Human pathway separately using Enrichr (Chen et al., 2013; Kuleshov et al., 2016; Xie et al., 2021) to find the relationship of our MwC map with disease pathways. We used the same gene list as the Metascape.

Synaptic density atlas

We used the high-resolution in vivo human brain synaptic density atlas provided by the Neurology Research Unit (NRU) at the University of Copenhagen (Johansen et al., 2024). This atlas was generated using PET imaging with [^{11}C]UCB-J, a radioligand that binds to synaptic vesicle glycoprotein 2A (SV2A) and provides quantitative estimates of synaptic density. Data were collected from 33 healthy adult participants (17 females, 16 males), aged 20-70 years (44.8 $\pm$ 14.6 years). The atlas represented the group-average synaptic density distribution across subjects. The in vivo PET data were calibrated to absolute concentration values (pmol/mL) using in vitro autoradiography from postmortem human brain tissue. Further details are described in Johansen et al. 2024.

Mitochondrial maps

We used mitochondrial phenotype maps from (Mosharov et al., 2025) that quantify regional mitochondrial density and respiratory capacity across the human brain. These maps were derived from a coronal slab of the right hemisphere of a 54-year-old neurotypical male, which was physically voxelized into 703 cubes (3 × 3 × 3 mm). Biochemical assays measured mitochondrial content (citrate synthase and mtDNA, combined into MitoD) and oxidative phosphorylation (OXPHOS) enzyme activities (averaged into TRC), from which a tissue-specific mitochondrial respiratory capacity map (MRC = TRC/MitoD) was computed. The maps were initially created in the native anatomical space of the donor brain and subsequently linearly registered to MNI ICBM152 space for neuroimaging compatibility. In our analysis, we resampled our MMP atlas to this MNI space and used it to parcellate the mitochondrial maps.

Amyloid-beta maps

We used amyloid PET data from the Alzheimer's Disease Neuroimaging Initiative (ADNI), provided by the authors of a recent study by (Roemer-Cassiano et al., 2025). PET scans were acquired using the AV45 (Florbetapir) tracer, registered to T1-weighted MRIs, and parcellated with the MMP1 atlas using a CAT12-based surface reconstruction pipeline. SUVR values were normalized to the whole cerebellum and extracted for cortical ROIs. To avoid longitudinal confounds, only the first available PET session per subject was included. The final dataset comprised 129 cognitively normal (CN) individuals (mean age = 75.5 ± 7.6 years; 83 females) and 95 individuals with mild cognitive impairment (MCI) (mean age = 76.0 ± 7.4 years; 41 females). These regional SUVR values were used to assess the spatial association between amyloid accumulation and MwC.

Data availability

All raw and preprocessed data from the TUM site are available in the OpenNeuro repository (https://openneuro.org/datasets/ds004513), the data from the Vienna site upon request. All derivative maps for the analyses are available on GitHub (https://github.com/NeuroenergeticsLab/metabolic_weighted_centrality). The 24 Neurosynth maps used in this study are also available on GitHub. Human gene expression data can be accessed via the Allen Human Brain Atlas database (http://human.brain-map.org/static/download). Synaptic density maps are described in (Johansen et al., 2024) and can be obtained from https://xtra.nru.dk/SV2A-atlas/. β-amyloid maps are described in (Roemer-Cassiano et al., 2025), and can be obtained from the corresponding authors.

Code availability

All scripts, Python Jupyter notebooks, and configuration files used to perform the analyses are available on GitHub (https://github.com/NeuroenergeticsLab/metabolic_weighted_centrality). The code for PLS analysis is available at https://github.com/SarahMorgan/Morphometric_Similarity_SZ. Gene enrichment analyses were performed using Metascape (https://metascape.org). KEGG analysis was conducted with Enrichr (https://maayanlab.cloud/Enrichr/).

Acknowledgements

We would like to thank Roman Belenya, Dr. Samira Epp, Antonia Bose, and André Hechler for their valuable input during the development of this idea. We thank Prof. Thomas Beyer and Lalith Kumar Shiyam Sundar for sharing the Vienna dataset and Dr. Nicolai Franzmeier for sharing the beta amyloid maps.

Funding

VR was funded by the European Research Council (ERC) under the European Union's Horizon 2020 research and innovation program (ERC Starting Grant, ID 759659).

Author contributions

MA designed and implemented the model, performed all analyses, and wrote the manuscript. LF provided guidance on transcriptomics and gene enrichment analyses, their biological interpretations, and revised the manuscript. GC provided supervision, guidance in data analysis and visualization, and revised the manuscript. VR conceptualized the study, contributed to model development, supervised the project, and wrote the manuscript.

Competing interests

The authors declare no competing interests.

REFERENCES

Abbasi, A., & Hossain, L. (2013). Hybrid Centrality Measures for Binary and Weighted Networks. In R. Menezes, A. Evsukoff, & M. C. González (Eds.), Complex Networks (Vol. 424, pp. 1–7). Springer Berlin Heidelberg. https://doi.org/10.1007/978-3-642-30287-9_1

Aiello, M., Salvatore, E., Cachia, A., Pappatà, S., Cavaliere, C., Prinster, A., Nicolai, E., Salvatore, M., Baron, J.-C., & Quarantelli, M. (2015). Relationship between simultaneously acquired resting-state regional cerebral glucose metabolism and functional MRI: A PET/MR hybrid scanner study. NeuroImage, 113, 111–121. https://doi.org/10.1016/j.neuroimage.2015.03.017

Arnemann, K. L., Stöber, F., Narayan, S., Rabinovici, G. D., & Jagust, W. J. (2018). Metabolic brain networks in aging and preclinical Alzheimer's disease. NeuroImage: Clinical, 17, 987–999. https://doi.org/10.1016/j.nicl.2017.12.037

Attwell, D., & Laughlin, S. B. (2001). An Energy Budget for Signaling in the Grey Matter of the Brain. Journal of Cerebral Blood Flow & Metabolism, 21(10), 1133–1145. https://doi.org/10.1097/00004647-200110000-00001

Bassett, D. S., & Sporns, O. (2017). Network neuroscience. Nature Neuroscience, 20(3), 353–364. https://doi.org/10.1038/nn.4502

Bazinet, V., Hansen, J. Y., & Misic, B. (2023). Towards a biologically annotated brain connectome. Nature Reviews Neuroscience, 24(12), 747–760. https://doi.org/10.1038/s41583-023-00752-3

Bijsterbosch, J., Harrison, S. J., Jbabdi, S., Woolrich, M., Beckmann, C., Smith, S., & Duff, E. P. (2020). Challenges and future directions for representations of functional brain organization. Nature Neuroscience, 23(12), 1484–1495. https://doi.org/10.1038/s41593-020-00726-z

Bobba-Alves, N., Sturm, G., Lin, J., Ware, S. A., Karan, K. R., Monzel, A. S., Bris, C., Procaccio, V., Lenaers, G., Higgins-Chen, A., Levine, M., Horvath, S., Santhanam, B. S., Kaufman, B. A., Hirano, M., Epel, E., & Picard, M. (2023). Cellular allostatic load is linked to increased energy expenditure and accelerated biological aging. Psychoneuroendocrinology, 155, 106322. https://doi.org/10.1016/j.psyneuen.2023.106322

Boccaletti, S., Bianconi, G., Criado, R., Del Genio, C. I., Gómez-Gardeñes, J., Romance, M., Sendiña-Nadal, I., Wang, Z., & Zanin, M. (2014). The structure and dynamics of multilayer networks. Physics Reports, 544(1), 1–122. https://doi.org/10.1016/j.physrep.2014.07.001

Bressler, S. L., & Menon, V. (2010). Large-scale brain networks in cognition: Emerging methods and principles. Trends in Cognitive Sciences, 14(6), 277–290. https://doi.org/10.1016/j.tics.2010.04.004

Buckner, R. L., Sepulcre, J., Talukdar, T., Krienen, F. M., Liu, H., Hedden, T., Andrews-Hanna, J. R., Sperling, R. A., & Johnson, K. A. (2009). Cortical Hubs Revealed by Intrinsic Functional Connectivity: Mapping, Assessment of Stability, and Relation to Alzheimer's Disease. The Journal of Neuroscience, 29(6), 1860–1873. https://doi.org/10.1523/JNEUROSCI.5062-08.2009

Bullmore, E., & Sporns, O. (2009). Complex brain networks: Graph theoretical analysis of structural and functional systems. Nature Reviews Neuroscience, 10(3), 186–198. https://doi.org/10.1038/nrn2575

Bullmore, E. T., & Bassett, D. S. (2011). Brain Graphs: Graphical Models of the Human Brain Connectome. Annual Review of Clinical Psychology, 7(1), 113–140. https://doi.org/10.1146/annurev-clinpsy-040510-143934

Burgos, N., Cardoso, M. J., Thielemans, K., Modat, M., Pedemonte, S., Dickson, J., Barnes, A., Ahmed, R., Mahoney, C. J., Schott, J. M., Duncan, J. S., Atkinson, D., Arridge, S. R., Hutton, B. F., & Ourselin, S. (2014). Attenuation Correction Synthesis for Hybrid PET-MR Scanners: Application to Brain Studies. IEEE Transactions on Medical Imaging, 33(12), 2332–2341. https://doi.org/10.1109/TMI.2014.2340135

Burt, J. B., Helmer, M., Shinn, M., Anticevic, A., & Murray, J. D. (2020). Generative modeling of brain maps with spatial autocorrelation. NeuroImage, 220, 117038. https://doi.org/10.1016/j.neuroimage.2020.117038

Castrillon, G., Epp, S., Bose, A., Fraticelli, L., Hechler, A., Belenya, R., Ranft, A., Yakushev, I., Utz, L., Sundar, L., Rauschecker, J. P., Preibisch, C., Kurcyus, K., & Riedl, V. (2023). An energy costly architecture of neuromodulators for human brain evolution and cognition. Science Advances, 9(50), eadi7632. https://doi.org/10.1126/sciadv.adi7632

Chen, E. Y., Tan, C. M., Kou, Y., Duan, Q., Wang, Z., Meirelles, G. V., Clark, N. R., & Ma'ayan, A. (2013). Enrichr: Interactive and collaborative HTML5 gene list enrichment analysis tool. BMC Bioinformatics, 14(1), 128. https://doi.org/10.1186/1471-2105-14-128

Cole, M. W., Pathak, S., & Schneider, W. (2010). Identifying the brain's most globally connected regions. NeuroImage, 49(4), 3132–3148. https://doi.org/10.1016/j.neuroimage.2009.11.001

Craddock, R. C., Jbabdi, S., Yan, C.-G., Vogelstein, J. T., Castellanos, F. X., Di Martino, A., Kelly, C., Heberlein, K., Colcombe, S., & Milham, M. P. (2013). Imaging human connectomes at the macroscale. Nature Methods, 10(6), 524–539. https://doi.org/10.1038/nmeth.2482

De Vico Fallani, F., Bassett, D., & Jiang, T. (2012). Graph Theoretical Approaches in Brain Networks. Computational and Mathematical Methods in Medicine, 2012, 1–2. https://doi.org/10.1155/2012/590483

Del Ferraro, G., Moreno, A., Min, B., Morone, F., Pérez-Ramírez, Ú., Pérez-Cervera, L., Parra, L. C., Holodny, A., Canals, S., & Makse, H. A. (2018). Finding influential nodes for integration in brain networks using optimal percolation theory. Nature Communications, 9(1), 2274. https://doi.org/10.1038/s41467-018-04718-3

Drew, P. J. (2022). Neurovascular coupling: Motive unknown. Trends in Neurosciences, 45(11), 809–819. https://doi.org/10.1016/j.tins.2022.08.004

Epp, S. M., Castrillón, G., Yuan, B., Andrews-Hanna, J., Preibisch, C., & Riedl, V. (2023). Two distinct modes of hemodynamic responses across the human cortex. Nature Neuroscience, in Press. https://doi.org/10.1101/2023.12.08.570806

Faskowitz, J., Esfahlani, F. Z., Jo, Y., Sporns, O., & Betzel, R. F. (2020). Edge-centric functional network representations of human cerebral cortex reveal overlapping system-level architecture. Nature Neuroscience, 23(12), 1644–1654. https://doi.org/10.1038/s41593-020-00719-y

Gajwani, M., Oldham, S., Pang, J. C., Arnatkevičiūtė, A., Tiego, J., Bellgrove, M. A., & Fornito, A. (2023). Can hubs of the human connectome be identified consistently with diffusion MRI? Network Neuroscience, 7(4), 1326–1350. https://doi.org/10.1162/netn_a_00324

Giustolisi, O., Ridolfi, L., & Simone, A. (2020). Embedding the intrinsic relevance of vertices in network analysis: The case of centrality metrics. Scientific Reports, 10(1), 3297. https://doi.org/10.1038/s41598-020-60151-x

Glasser, M. F., Coalson, T. S., Robinson, E. C., Hacker, C. D., Harwell, J., Yacoub, E., Ugurbil, K., Andersson, J., Beckmann, C. F., Jenkinson, M., Smith, S. M., & Van Essen, D. C. (2016). A multi-modal parcellation of human cerebral cortex. Nature, 536(7615), 171–178. https://doi.org/10.1038/nature18933

Hagmann, P., Cammoun, L., Gigandet, X., Meuli, R., Honey, C. J., Wedeen, V. J., & Sporns, O. (2008). Mapping the Structural Core of Human Cerebral Cortex. PLoS Biology, 6(7), e159. https://doi.org/10.1371/journal.pbio.0060159

Hansen, J. Y., Shafiei, G., Voigt, K., Liang, E. X., Cox, S. M. L., Leyton, M., Jamadar, S. D., & Misic, B. (2023). Integrating multimodal and multiscale connectivity blueprints of the human cerebral cortex in health and disease. PLOS Biology, 21(9), e3002314. https://doi.org/10.1371/journal.pbio.3002314

Harris, J. J., Jolivet, R., & Attwell, D. (2012). Synaptic Energy Use and Supply. Neuron, 75(5), 762–777. https://doi.org/10.1016/j.neuron.2012.08.019

Hawrylycz, M. J., Lein, E. S., Guillozet-Bongaarts, A. L., Shen, E. H., Ng, L., Miller, J. A., van de Lagemaat, L. N., Smith, K. A., Ebbert, A., Riley, Z. L., Abajian, C., Beckmann, C. F., Bernard, A., Bertagnolli, D., Boe, A. F., Cartagena, P. M., Chakravarty, M. M., Chapin, M., Chong, J., ...

Jones, A. R. (2012). An anatomically comprehensive atlas of the adult human brain transcriptome. Nature, 489(7416), 391–399. https://doi.org/10.1038/nature11405
Heitzig, J., Donges, J. F., Zou, Y., Marwan, N., & Kurths, J. (2012). Node-weighted measures for complex networks with spatially embedded, sampled, or differently sized nodes. The European Physical Journal B, 85(1), 38. https://doi.org/10.1140/epjb/e2011-20678-7
Hoge, R. D., & Pike, G. B. (2001). Oxidative metabolism and the detection of neuronal activation via imaging. Journal of Chemical Neuroanatomy, 22(1), 43–52. https://doi.org/10.1016/S0891-0618(01)00114-4
Howarth, C., Mishra, A., & Hall, C. N. (2020). More than just summed neuronal activity: How multiple cell types shape the BOLD response. Philosophical Transactions of the Royal Society B: Biological Sciences, 376(1815), 20190630. https://doi.org/10.1098/rstb.2019.0630
Hyder, F., & Rothman, D. L. (2010). Neuronal correlate of BOLD signal fluctuations at rest: Err on the side of the baseline. Proceedings of the National Academy of Sciences, 107(24), 10773–10774. https://doi.org/10.1073/pnas.1005135107
Hyder, F., Rothman, D. L., & Bennett, M. R. (2013). Cortical energy demands of signaling and nonsignaling components in brain are conserved across mammalian species and activity levels. Proceedings of the National Academy of Sciences, 110(9), 3549–3554. https://doi.org/10.1073/pnas.1214912110
Ince, R. A. A., Giordano, B. L., Kayser, C., Rousselet, G. A., Gross, J., & Schyns, P. G. (2017). A statistical framework for neuroimaging data analysis based on mutual information estimated via a gaussian copula. Human Brain Mapping, 38(3), 1541–1573. https://doi.org/10.1002/hbm.23471
Johansen, A., Beliveau, V., Colliander, E., Raval, N. R., Dam, V. H., Gillings, N., Aznar, S., Svarer, C., Plavén-Sigray, P., & Knudsen, G. M. (2024). An In Vivo High-Resolution Human Brain Atlas of Synaptic Density. The Journal of Neuroscience, 44(33), e1750232024. https://doi.org/10.1523/JNEUROSCI.1750-23.2024
Karbowski, J. (2012). Approximate Invariance of Metabolic Energy per Synapse during Development in Mammalian Brains. PLoS ONE, 7(3), e33425. https://doi.org/10.1371/journal.pone.0033425
Kivela, M., Arenas, A., Barthelemy, M., Gleeson, J. P., Moreno, Y., & Porter, M. A. (2014). Multilayer networks. Journal of Complex Networks, 2(3), 203–271. https://doi.org/10.1093/comnet/cnu016
Kuhnert, M.-T., Geier, C., Elger, C. E., & Lehnertz, K. (2012). Identifying important nodes in weighted functional brain networks: A comparison of different centrality approaches. Chaos: An Interdisciplinary Journal of Nonlinear Science, 22(2), 023142. https://doi.org/10.1063/1.4729185
Kuleshov, M. V., Jones, M. R., Rouillard, A. D., Fernandez, N. F., Duan, Q., Wang, Z., Koplev, S., Jenkins, S. L., Jagodnik, K. M., Lachmann, A., McDermott, M. G., Monteiro, C. D., Gundersen, G. W., & Ma'ayan, A. (2016). Enrichr: A comprehensive gene set enrichment analysis web server 2016 update. Nucleic Acids Research, 44(W1), W90–W97. https://doi.org/10.1093/nar/gkw377
Kwon, H., Choi, Y.-H., & Lee, J.-M. (2019). A Physarum Centrality Measure of the Human Brain Network. Scientific Reports, 9(1), 5907. https://doi.org/10.1038/s41598-019-42322-7
Liao, X.-H., Xia, M.-R., Xu, T., Dai, Z.-J., Cao, X.-Y., Niu, H.-J., Zuo, X.-N., Zang, Y.-F., & He, Y. (2013). Functional brain hubs and their test–retest reliability: A multiband resting-state functional MRI study. NeuroImage, 83, 969–982. https://doi.org/10.1016/j.neuroimage.2013.07.058
Lin, H., Pan, T., Min Wang, Ge, J., Lu, J., Ju, Z., Chen, K., Zhang, H., Guan, Y., Zhao, Q., Shan, B., Nie, B., Zuo, C., & Wu, P. (2023). Metabolic Asymmetry Relates to Clinical Characteristics and Brain Network Abnormalities in Alzheimer's Disease. Journal of Alzheimer's Disease, 93(4), 1395–1406. https://doi.org/10.3233/JAD-221258
Liu, Z.-Q., Luppi, A. I., Hansen, J. Y., Tian, Y. E., Zalesky, A., Yeo, B. T. T., Fulcher, B. D., & Misic, B. (2025). Benchmarking methods for mapping functional connectivity in the brain. Nature Methods, 22(7), 1593–1602. https://doi.org/10.1038/s41592-025-02704-4

Margulies, D. S., Ghosh, S. S., Goulas, A., Falkiewicz, M., Huntenburg, J. M., Langs, G., Bezgin, G., Eickhoff, S. B., Castellanos, F. X., Petrides, M., Jefferies, E., & Smallwood, J. (2016). Situating the default-mode network along a principal gradient of macroscale cortical organization. Proceedings of the National Academy of Sciences, 113(44), 12574–12579. https://doi.org/10.1073/pnas.1608282113

Markello, R. D., Arnatkeviciute, A., Poline, J.-B., Fulcher, B. D., Fornito, A., & Misic, B. (2021). Standardizing workflows in imaging transcriptomics with the abagen toolbox. eLife, 10, e72129. https://doi.org/10.7554/eLife.72129

Markiewicz, P. J., Ehrhardt, M. J., Erlandsson, K., Noonan, P. J., Barnes, A., Schott, J. M., Atkinson, D., Arridge, S. R., Hutton, B. F., & Ourselin, S. (2018). NiftyPET: A High-throughput Software Platform for High Quantitative Accuracy and Precision PET Imaging and Analysis. Neuroinformatics, 16(1), 95–115. https://doi.org/10.1007/s12021-017-9352-y

Menon, V. (2011). Large-scale brain networks and psychopathology: A unifying triple network model. Trends in Cognitive Sciences, 15(10), 483–506. https://doi.org/10.1016/j.tics.2011.08.003

Morella, I. M., Brambilla, R., & Morè, L. (2022). Emerging roles of brain metabolism in cognitive impairment and neuropsychiatric disorders. Neuroscience & Biobehavioral Reviews, 142, 104892. https://doi.org/10.1016/j.neubiorev.2022.104892

Morgan, S. E., Seidlitz, J., Whitaker, K. J., Romero-Garcia, R., Clifton, N. E., Scarpazza, C., Van Amelsvoort, T., Marcelis, M., Van Os, J., Donohoe, G., Mothersill, D., Corvin, A., Pocklington, A., Raznahan, A., McGuire, P., Vértes, P. E., & Bullmore, E. T. (2019). Cortical patterning of abnormal morphometric similarity in psychosis is associated with brain expression of schizophrenia-related genes. Proceedings of the National Academy of Sciences, 116(19), 9604–9609. https://doi.org/10.1073/pnas.1820754116

Mosharov, E. V., Rosenberg, A. M., Monzel, A. S., Osto, C. A., Stiles, L., Rosoklija, G. B., Dwork, A. J., Bindra, S., Junker, A., Zhang, Y., Fujita, M., Mariani, M. B., Bakalian, M., Sulzer, D., De Jager, P. L., Menon, V., Shirihai, O. S., Mann, J. J., Underwood, M. D., … Picard, M. (2025). A human brain map of mitochondrial respiratory capacity and diversity. Nature, 641(8063), 749–758. https://doi.org/10.1038/s41586-025-08740-6

Murphy, A. C., Gu, S., Khambhati, A. N., Wymbs, N. F., Grafton, S. T., Satterthwaite, T. D., & Bassett, D. S. (2016). Explicitly Linking Regional Activation and Function Connectivity: Community Structure of Weighted Networks with Continuous Annotation (Version 1). arXiv. https://doi.org/10.48550/ARXIV.1611.07962

Nijhuis, E. H. J., Van Cappellen Van Walsum, A.-M., & Norris, D. G. (2013). Topographic Hub Maps of the Human Structural Neocortical Network. PLoS ONE, 8(6), e65511. https://doi.org/10.1371/journal.pone.0065511

Park, H.-J., & Friston, K. (2013). Structural and Functional Brain Networks: From Connections to Cognition. Science, 342(6158), 1238411. https://doi.org/10.1126/science.1238411

Patlak, C. S., & Blasberg, R. G. (1985). Graphical Evaluation of Blood-to-Brain Transfer Constants from Multiple-Time Uptake Data. Generalizations. Journal of Cerebral Blood Flow & Metabolism, 5(4), 584–590. https://doi.org/10.1038/jcbfm.1985.87

Peterson, K. L., Sanchez-Romero, R., Mill, R. D., & Cole, M. W. (2025). Regularized partial correlation provides reliable functional connectivity estimates while correcting for widespread confounding. Imaging Neuroscience. https://doi.org/10.1162/IMAG.a.162

Power, J. D., Cohen, A. L., Nelson, S. M., Wig, G. S., Barnes, K. A., Church, J. A., Vogel, A. C., Laumann, T. O., Miezin, F. M., Schlaggar, B. L., & Petersen, S. E. (2011). Functional Network Organization of the Human Brain. Neuron, 72(4), 665–678. https://doi.org/10.1016/j.neuron.2011.09.006

Power, J. D., Schlaggar, B. L., Lessov-Schlaggar, C. N., & Petersen, S. E. (2013). Evidence for Hubs in Human Functional Brain Networks. Neuron, 79(4), 798–813. https://doi.org/10.1016/j.neuron.2013.07.035

Preti, M. G., & Van De Ville, D. (2019). Decoupling of brain function from structure reveals regional behavioral specialization in humans. Nature Communications, 10(1), 4747. https://doi.org/10.1038/s41467-019-12765-7

Roemer-Cassiano, S. N., Wagner, F., Evangelista, L., Rauchmann, B.-S., Dehsarvi, A., Steward, A., Dewenter, A., Biel, D., Zhu, Z., Pescoller, J., Gross, M., Perneczky, R., Malpetti, M., Ewers, M., Schöll, M., Dichgans, M., Höglinger, G. U., Brendel, M., Jäkel, S., & Franzmeier, N. (2025). Amyloid-associated hyperconnectivity drives tau spread across connected brain regions in Alzheimer's disease. Science Translational Medicine, 17(782). https://doi.org/10.1126/scitranslmed.adp2564

Rosvall, M., & Bergstrom, C. T. (2008). Maps of random walks on complex networks reveal community structure. Proceedings of the National Academy of Sciences, 105(4), 1118–1123. https://doi.org/10.1073/pnas.0706851105

Rubinov, M., & Sporns, O. (2010). Complex network measures of brain connectivity: Uses and interpretations. NeuroImage, 52(3), 1059–1069. https://doi.org/10.1016/j.neuroimage.2009.10.003

Sanabria-Diaz, G., Martínez-Montes, E., Melie-Garcia, L., & the Alzheimer's Disease Neuroimaging Initiative. (2013). Glucose Metabolism during Resting State Reveals Abnormal Brain Networks Organization in the Alzheimer's Disease and Mild Cognitive Impairment. PLoS ONE, 8(7), e68860. https://doi.org/10.1371/journal.pone.0068860

Scholtens, L. H., Pijnenburg, R., de Lange, S. C., Huitinga, I., & van den Heuvel, M. P. (2022). Common Microscale and Macroscale Principles of Connectivity in the Human Brain. The Journal of Neuroscience, 42(20), 4147–4163. https://doi.org/10.1523/JNEUROSCI.1572-21.2022

Sercel, A. J., Sturm, G., Gallagher, D., St-Onge, M.-P., Kempes, C. P., Pontzer, H., Hirano, M., & Picard, M. (2024). Hypermetabolism and energetic constraints in mitochondrial disorders. Nature Metabolism, 6(2), 192–195. https://doi.org/10.1038/s42255-023-00968-8

Shine, J. M., Breakspear, M., Bell, P. T., Ehgoetz Martens, K., Shine, R., Koyejo, O., Sporns, O., & Poldrack, R. A. (2019). Human cognition involves the dynamic integration of neural activity and neuromodulatory systems. Nature Neuroscience, 22(2), 289–296. https://doi.org/10.1038/s41593-018-0312-0

Simpson, E. H. (1949). Measurement of Diversity. Nature, 163(4148), 688–688. https://doi.org/10.1038/163688a0

Singh, A., Singh, R. R., & Iyengar, S. R. S. (2020). Node-weighted centrality: A new way of centrality hybridization. Computational Social Networks, 7(1), 6. https://doi.org/10.1186/s40649-020-00081-w

Smith, D. M., Kraus, B. T., Dworetsky, A., Gordon, E. M., & Gratton, C. (2023). Brain hubs defined in the group do not overlap with regions of high inter-individual variability. NeuroImage, 277, 120195. https://doi.org/10.1016/j.neuroimage.2023.120195

Sporns, O. (2011). The human connectome: A complex network: The human connectome. Annals of the New York Academy of Sciences, 1224(1), 109–125. https://doi.org/10.1111/j.1749-6632.2010.05888.x

Sporns, O. (2018). Graph theory methods: Applications in brain networks. Dialogues in Clinical Neuroscience, 20(2), 111–121. https://doi.org/10.31887/DCNS.2018.20.2/osporns

Steiger, J. H. (1980). Tests for comparing elements of a correlation matrix. Psychological Bulletin, 87(2), 245–251. https://doi.org/10.1037/0033-2909.87.2.245

Sundar, L. K., Muzik, O., Rischka, L., Hahn, A., Rausch, I., Lanzenberger, R., Hienert, M., Klebermass, E.-M., Füchsel, F.-G., Hacker, M., Pilz, M., Pataraia, E., Traub-Weidinger, T., & Beyer, T. (2019). Towards quantitative [18F]FDG-PET/MRI of the brain: Automated MR-driven calculation of an image-derived input function for the non-invasive determination of cerebral glucose metabolic rates. Journal of Cerebral Blood Flow & Metabolism, 39(8), 1516–1530. https://doi.org/10.1177/0271678X18776820

Thomas Yeo, B. T., Krienen, F. M., Sepulcre, J., Sabuncu, M. R., Lashkari, D., Hollinshead, M., Roffman, J. L., Smoller, J. W., Zöllei, L., Polimeni, J. R., Fischl, B., Liu, H., & Buckner, R. L. (2011). The organization of the human cerebral cortex estimated by intrinsic functional connectivity. Journal of Neurophysiology, 106(3), 1125–1165. https://doi.org/10.1152/jn.00338.2011

Tomasi, D., & Volkow, N. D. (2011). Functional connectivity hubs in the human brain. NeuroImage, 57(3), 908–917. https://doi.org/10.1016/j.neuroimage.2011.05.024

Tournier, J.-D., Smith, R., Raffelt, D., Tabbara, R., Dhollander, T., Pietsch, M., Christiaens, D., Jeurissen, B., Yeh, C.-H., & Connelly, A. (2019). MRtrix3: A fast, flexible and open software framework for medical image processing and visualisation. NeuroImage, 202, 116137. https://doi.org/10.1016/j.neuroimage.2019.116137

Van Den Heuvel, M. P., & Sporns, O. (2013). Network hubs in the human brain. Trends in Cognitive Sciences, 17(12), 683–696. https://doi.org/10.1016/j.tics.2013.09.012

Wang, B., Zhang, J., Dai, J., & Sheng, J. (2022). Influential nodes identification using network local structural properties. Scientific Reports, 12(1), 1833. https://doi.org/10.1038/s41598-022-05564-6

Watts, M. E., Pocock, R., & Claudianos, C. (2018). Brain Energy and Oxygen Metabolism: Emerging Role in Normal Function and Disease. Frontiers in Molecular Neuroscience, 11, 216. https://doi.org/10.3389/fnmol.2018.00216

Wiedermann, M., Donges, J. F., Heitzig, J., & Kurths, J. (2013). Node-weighted interacting network measures improve the representation of real-world complex systems. EPL (Europhysics Letters), 102(2), 28007. https://doi.org/10.1209/0295-5075/102/28007

Wu, H. (2003). Measurement of the Global Lumped Constant for 2-Deoxy-2-[18F]Fluoro-D-Glucose in Normal Human Brain Using [15O]Water and 2-Deoxy-2-[18F]Fluoro-D-Glucose Positron Emission Tomography Imaging A Method with Validation Based on Multiple Methodologies. Molecular Imaging & Biology, 5(1), 32–41. https://doi.org/10.1016/S1536-1632(02)00122-1

Xie, Z., Bailey, A., Kuleshov, M. V., Clarke, D. J. B., Evangelista, J. E., Jenkins, S. L., Lachmann, A., Wojciechowicz, M. L., Kropiwnicki, E., Jagodnik, K. M., Jeon, M., & Ma'ayan, A. (2021). Gene Set Knowledge Discovery with Enrichr. Current Protocols, 1(3), e90. https://doi.org/10.1002/cpz1.90

Yang, J., Hu, C., Guo, N., Dutta, J., Vaina, L. M., Johnson, K. A., Sepulcre, J., Fakhri, G. E., & Li, Q. (2017). Partial volume correction for PET quantification and its impact on brain network in Alzheimer's disease. Scientific Reports, 7(1), 13035. https://doi.org/10.1038/s41598-017-13339-7

Yarkoni, T., Poldrack, R. A., Nichols, T. E., Van Essen, D. C., & Wager, T. D. (2011). Large-scale automated synthesis of human functional neuroimaging data. Nature Methods, 8(8), 665–670. https://doi.org/10.1038/nmeth.1635

Zalesky, A., Fornito, A., & Bullmore, E. T. (2010). Network-based statistic: Identifying differences in brain networks. NeuroImage, 53(4), 1197–1207. https://doi.org/10.1016/j.neuroimage.2010.06.041

Zamani Esfahlani, F., Bertolero, M. A., Bassett, D. S., & Betzel, R. F. (2020). Space-independent community and hub structure of functional brain networks. NeuroImage, 211, 116612. https://doi.org/10.1016/j.neuroimage.2020.116612

Zhang, J., Scholtens, L. H., Wei, Y., Van Den Heuvel, M. P., Chanes, L., & Barrett, L. F. (2020). Topography Impacts Topology: Anatomically Central Areas Exhibit a "High-Level Connector" Profile in the Human Cortex. Cerebral Cortex, 30(3), 1357–1365. https://doi.org/10.1093/cercor/bhz171

Zhang, X.-H., Anderson, K. M., Dong, H.-M., Chopra, S., Dhamala, E., Emani, P. S., Gerstein, M. B., Margulies, D. S., & Holmes, A. J. (2024). The cell-type underpinnings of the human functional cortical connectome. Nature Neuroscience, 1–11. https://doi.org/10.1038/s41593-024-01812-2

Zhou, Y., Zhou, B., Pache, L., Chang, M., Khodabakhshi, A. H., Tanaseichuk, O., Benner, C., & Chanda, S. K. (2019). Metascape provides a biologist-oriented resource for the analysis of systems-level datasets. Nature Communications, 10(1), 1523. https://doi.org/10.1038/s41467-019-09234-6

Zuo, X.-N., Ehmke, R., Mennes, M., Imperati, D., Castellanos, F. X., Sporns, O., & Milham, M. P. (2012). Network Centrality in the Human Functional Connectome. Cerebral Cortex, 22(8), 1862–1875. https://doi.org/10.1093/cercor/bhr269